Communication

Hybrid Electromagnetic Inversion of 3-D Irregular Scatterers Embedded in Layered Media by VBIM and MET

Xianliang Huang, Jiawen Li, Yanjin Chen, Feng Han, and Qing Huo Liu

***Abstract*— This communication presents an efficient hybrid nonlinear electromagnetic inversion method. The voxel-based variational Born iterative method (VBIM) is combined with the maximum entropy thresholding (MET) technique to reconstruct 3-D irregular scatterers embedded in the layered media. In each iteration, the VBIM first outputs the model parameters in discretized cells of the inversion domain, and the MET is then used to categorize them into "background" and "scatterer" types. Partial "background" cells will be removed in the next round iteration according to an adjustable threshold corresponding to the maximum entropy since they have no contribution to the measured scattered fields. Consequently, the inversion domain is gradually downsized in the successive iterations. The computation efficiency, memory cost, and the reconstruction accuracy are compared for VBIM with and without the MET. Their antinoise ability is also compared.**

***Index Terms*— Electromagnetic (EM) inversion, maximum entropy thresholding (MET), variational Born iterative method (VBIM).**

I. Introduction

Electromagnetic (EM) inversion is to retrieve several model parameters such as positions, shapes, and dielectric properties of scatterers located in a region of interest from the measured EM data. Over the past decades, various EM inversion methods have been successfully applied to biomedical imaging [1], nondestructive inspection [2], through-wall imaging [3], and geophysical remote sensing [4].

According to the availability of *a priori* information of the model parameters in the inversion domain, the EM inversion methods can be categorized into two kinds, the model based and the voxel based. In the model-based inversion, a partial *a priori* information of the unknown model parameter distribution in the inversion domain can be obtained in advance. As a result, the dimension of the vector of unknowns in the final discretized data equation can be immediately reduced or reduced in a transformed domain. This advantage helps to mitigate the ill-posedness of the inverse problem, save computation cost, and acquire more accurate solutions. In the previous works, several model-based inversion methods have been discussed [5]–[7], and their applications in geophysical exploration [8], reconstruction of 3-D anisotropic objects [9], optoacoustic tomography [10], etc., were also demonstrated. However, the model-based inversion usually requires that we know the general locations, approximate shapes, or even the mathematical formulas to express the topologies of the scatterers in the inversion domain before implementing the iterations. Unfortunately, these requirements cannot be satisfied in many real-world applications.

On the other hand, the voxel-based inversion directly solves for all the model parameter values of all the discretized cells in the inversion domain without incorporating any *a priori* information. One popular scheme to describe the voxel-based EM inversion is using the state and data equations [11] based on the integral equation method. In this framework, many iterative methods such as Born iteration method (BIM) and its variants [12], [13], contrast source inversion (CSI) [14], and subspace optimization method (SOM) [15] have been developed. When BIM, variational BIM (VBIM), or distorted BIM (DBIM) is adopted to solve an inverse problem, the state and data equations are solved alternately [12], [13]. The final reconstructed model parameters in all the discretized cells are solved from the data equation when the data misfits of the computed fields reduce to a prescribed criterion. Different from BIM, CSI has no forward computation; its cost function is constructed using the summation of mismatches in the data equation, and the state equation and the contrast source are updated alternately [16]. SOM is implemented similar to CSI but for a subspace of the induced current. Compared with the model-based inversion methods, these voxel-based full-wave inversion methods are more competent for the reconstruction of scatterers with irregular shapes and arbitrary parameter distributions. However, the computation cost is usually rather expensive in the voxel-based inversion due to the large dimension of the unknown vector in the discretized data equation.

In this communication, we propose a hybrid full-wave EM inversion method to take the advantage of the merit of voxel-based inversion while significantly reducing the dimension of the vector of unknowns. As mentioned above, because the model parameters in the inversion domain are directly reduced or reduced in a transformed domain by the aid of partial *a priori* information, the model-based inversion can effectively save the computation cost. Therefore, we try to reduce the number of model parameters in the voxel-based inversion. Several methods have been proposed in the previous works. The first kind is to utilize the *a priori* information of the "sparsity" of the scatterers. In this situation, the scatterers only take a rather limited number of discretized cells. The noniterative method compressive sensing (CS) has been proposed to reconstruct both the shapes and dielectric parameters of the sparse scatterers [17], [18]. The second kind is to explore the *a priori* information iteratively. In other words, the iterative full-wave inversion is implemented several rounds. The reconstructed results in the current round provide some information of the unknown scatterers for the next round. The representative method is the iterative multiscaling approach (IMSA) [19], [20]. After each round of iterations is complete, the inversion domain is zoomed in, and the finer discretized cells will be used in the next round. As a result, the reconstructed results with multiple resolutions can be obtained. In this article, we do not make use of any *a priori* information and only know the whole inversion domain

Manuscript received January 7, 2020; revised March 2, 2020; accepted March 29, 2020. Date of publication April 9, 2020; date of current version December 17, 2020. This work was supported by the National Key Research and Development Program of the Ministry of Science and Technology of China under Grant 2018YFC0603503 and Grant 2018YFF01013300. *(Corresponding authors: Feng Han; Qing Huo Liu.)*

Xianliang Huang, Jiawen Li, Yanjin Chen, and Feng Han are with the Fujian Provincial Key Laboratory of Electromagnetic Wave Science and Detection Technology, Institute of Electromagnetics and Acoustics, Xiamen University, Xiamen 361005, China (e-mail: feng.han@xmu.edu.cn).

Qing Huo Liu is with the Department of Electrical and Computer Engineering, Duke University, Durham, NC 27708 USA (e-mail: qhliu@duke.edu).

Color versions of one or more of the figures in this communication are available online at https://ieeexplore.ieee.org.

Digital Object Identifier 10.1109/TAP.2020.2985156

including the "background" subregion and "scatterer" subregion. Note that the reconstructed model parameters in all the discretized cells in the inversion domain are analogous to gray levels of pixels in a 2-D image. The cells belonging to the background medium in the inversion domain are similar to the background pixels in the image. The scatterers enclosed in the inversion domain are similar to the objects in the image. The "background" cells in voxel-based EM inversion have no contribution to the scattered fields. If we can segment the "scatterer" cells and "background" cells in the inversion domain and gradually remove the "background" cells in each iteration, the dimension of the vector of unknowns in the discretized data equation can be effectively reduced. As no any *a priori* information of the scatterers is provided, we adopt the mature image segmentation method and maximum entropy thresholding (MET) [21], [22], to distinguish the "scatterer" cells and "background" cells in each iteration, and remove the "background" cells as well. Here, the word "remove" means that the model parameters in these cells are directly assigned as the background medium parameters, and they will not be assembled into the discretized matrix equation. In this way, the inversion domain is downsized, and the dimension of the vector of unknowns is reduced. This proposed method is different from IMSA in three aspects.

1) The discretization of the inversion domain is fixed in the proposed method while it is dynamically adjusted in the IMSA.
2) The iterations of full-wave inversion are only implemented one round in the proposed method, but they are implemented several rounds in the IMSA.
3) Multiple resolution inversion results are acquired in the IMSA, but the resolution is fixed in the proposed method.

The innovation of this communication is that we combine the voxel-based full-wave inversion with the statistical algorithm MET to reconstruct the model parameters of scatterers with low computational cost. As VBIM converges faster than BIM but has no need to update the Green's functions as in the DBIM, it is employed in this communication. However, we want to emphasize that other voxel-based inversion methods such as CSI or SOM also can be hybridized with MET. This communication is organized as follows. In Section II, we briefly describe the state and data equations used to solve the inverse scattering problem. Then, the procedure for applying the MET to VBIM results to segment the "scatterer" cells from the "background" cells is discussed in detail. The hybridization of VBIM and MET is also shown in a flowchart. In Section III, numerical examples are used to verify the proposed hybrid inversion method. Its performance and antinoise ability are also evaluated. In Section IV, the conclusions are drawn.

II. Methods

A. Forward and Inversion Models

If the electric field integral equation (EFIE) is used to solve the EM scattering problem, the forward model is formulated by the state equation which can be expressed as [23]

$$\mathbf{E}_{in}^{m} = \mathbf{E}_{tot}^{m} - j\omega\varepsilon_b \int_D \overline{\overline{\mathbf{G}}}_{\mathbf{EJ}}^{mm}(\mathbf{r},\mathbf{r}') \cdot \chi(\mathbf{r}')\mathbf{E}_{tot}^{m}(\mathbf{r}')d\mathbf{r}' \tag{1}$$

where $\chi = (\varepsilon - \varepsilon_b/\varepsilon_b)$ is the contrast function of the scatterers, and ε_b is the permittivity of the background medium.

The inversion model is formulated by the data equation [23], [24] which can be expressed as

$$\mathbf{E}_{sct}^{n}(\mathbf{r}) = j\omega\varepsilon_b \int_D \overline{\overline{\mathbf{G}}}_{\mathbf{EJ}}^{nm}(\mathbf{r},\mathbf{r}') \cdot \chi(\mathbf{r}')\mathbf{E}_{tot}^{m}(\mathbf{r}')d\mathbf{r}' \tag{2a}$$

$$\mathbf{H}_{sct}^{n}(\mathbf{r}) = j\omega\varepsilon_b \int_D \overline{\overline{\mathbf{G}}}_{\mathbf{HJ}}^{nm}(\mathbf{r},\mathbf{r}') \cdot \chi(\mathbf{r}')\mathbf{E}_{tot}^{m}(\mathbf{r}')d\mathbf{r}' \tag{2b}$$

where $\overline{\overline{\mathbf{G}}}_{\mathbf{EJ}}^{nm}$ and $\overline{\overline{\mathbf{G}}}_{\mathbf{HJ}}^{nm}$ are the dyadic Green's functions (DGFs) of the layered medium [25] connecting the equivalent electric current sources in the mth layer and the receivers in the nth layer, and D is the inversion domain enclosing the scatterers and located in the mth layer.

In the forward scattering computation, we solve for $\mathbf{E}_{tot}^{m}$ in (1) by the stabilized biconjugate gradient fast Fourier transform (BCGS-FFT) [26]. In the inverse scattering computation, (2) is discretized, and the model parameter χ is solved by VBIM [24]. This alternate iteration continues until the misfit between the measured scattered field and the calculated field reaches a stop criterion.

B. MET Applied to VBIM Results

Solving an inverse problem is using some measurements of the observable parameters to infer the values of model parameters. The voxel-based VBIM outputs the model parameters for the discretized cells in the inversion domain. Due to the underdetermined nature of the discretized matrix equation from the data equation (2), the reconstructed model parameters in the discretized cells are pseudorandom. As no *a priori* information is provided in the voxel-based inversion, we can divide the inversion domain into the "background" subregion and "scatterer" subregion but retain the maximum uncertainty. MET is an appropriate choice which has been validated by image segmentation [22]. We redefine a positive new contrast $\chi' = |\varepsilon - \varepsilon_b|$, where ε is the reconstructed permittivity in a certain discretized cell and ε_b is the known permittivity of the background medium. Assuming that the reconstructed χ' in all the discretized cells of the inversion domain varies from χ'_{min} to χ'_{max}, we divide the length $\chi'_{max} - \chi'_{min}$ with an appropriate equidistant interval into M subintervals. The probability of the contrast χ' in the ith subinterval is defined as

$$p(\chi'_i) = \frac{N(i)}{N_x \times N_y \times N_z} \tag{3}$$

where $N(i)$ is the total number of discretized cells falling into the ith subinterval. N_x, N_y, and N_z are the numbers of discretized cells in the x, y, and z direction of the inversion domain, respectively.

Given the qth subinterval, $p_b(q)$ and $p_s(q)$ denote the cumulative probability of background contrast χ'_b and scatterer contrast χ'_s for the qth threshold segmentation, respectively. They are calculated by

$$p_b(q) = \sum_{i=0}^{q} p(\chi'_i) \tag{4a}$$

$$p_s(q) = \sum_{i=q+1}^{M} p(\chi'_i). \tag{4b}$$

We then evaluate the conditional probability of χ'_i in each subinterval with respect to the background χ'_b and scatterer χ'_s as

$$p(\chi'_i|\chi'_i \in \chi'_b) = \frac{p(\chi'_i)}{p_b(q)}, \quad i = 1, \ldots, q \tag{5a}$$

$$p(\chi'_i|\chi'_i \in \chi'_s) = \frac{p(\chi'_i)}{p_s(q)}, \quad i = q+1, q+2, \ldots, M. \tag{5b}$$

The total entropy of the background and scatterer is calculated by

$$H_b(q) = -\sum_{i=1}^{q} p(\chi'_i|\chi'_i \in \chi'_b) \log p(\chi'_i|\chi'_i \in \chi'_b) \tag{6a}$$

$$H_s(q) = -\sum_{i=q+1}^{M} p(\chi'_i|\chi'_i \in \chi'_s) \log p(\chi'_i|\chi'_i \in \chi'_s). \tag{6b}$$

We maximize the total entropy

$$H_{tot}(q) = H_b(q) + H_s(q) \tag{7}$$

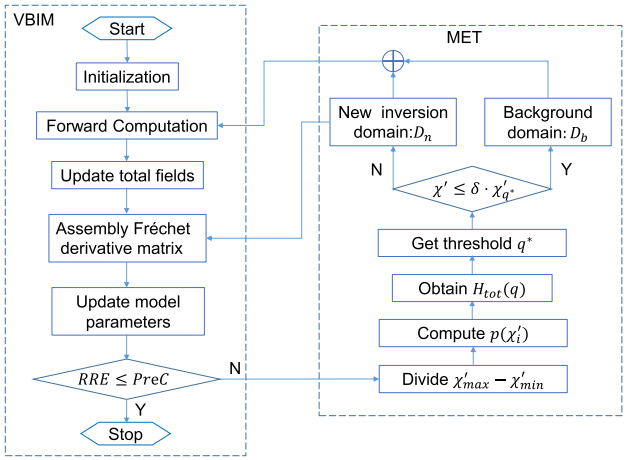

Fig. 1. Flowchart of hybridization of VBIM and MET. VBIM iterations stop when the relative residual error (RRE) of the computed scattered field with respect to the measured field is less than the threshold $PreC$. δ is a prescribed ratio to control the removal of the "background" cells.

and obtain the threshold index

$$q^* = \arg\max_{1 \le q \le M} H_{tot}(q). \tag{8}$$

The segmentation index threshold q^* corresponding to the maximum entropy is taken as the final classification threshold. The discretized cells in the subintervals with the indexes larger than q^* are determined as the "scatterer" cells, whereas the cells in the subintervals with the indexes smaller than or equal to the threshold q^* are determined as the "background" cells. These "background" cells will be partially removed in the next VBIM iteration to reduce the dimension of the unknown vector in the discretized data equation.

C. Hybridization of VBIM and MET

As mentioned above, the major purpose of MET is to classify the reconstructed model parameters of all the discretized cells into "background" and "scatterer" ones. When there are multiple model parameters in each cell, a cell can be judged as the "background" cell only if all the model parameters in this cell satisfy the "background" criterion. For example, if there are two parameters, the permittivity ϵ and conductivity σ, their respective threshold is written as

$$q^*_\epsilon = \arg\max H^{\epsilon}_{tot}(q) \tag{9a}$$

$$q^*_\sigma = \arg\max H^{\sigma}_{tot}(q). \tag{9b}$$

Only when $i < min\{q^*_\epsilon, q^*_\sigma\}$ cells in the ith subinterval can be confirmed as "backgound" ones. Fig. 1 shows the flowchart of the hybridization between VBIM and MET. In each iteration, the reconstructed model parameters of discretized cells in the inversion domain are classified by MET. Since the "background" cells have no contribution to the scattered fields, they can be removed in the next round inverse scattering computation. However, MET is a statistical method. Some "scatterer" cells may be incorrectly judged as "background" cells and removed. Therefore, we set a ratio δ to control the threshold and treat a certain discretized cell in the inversion domain satisfying

$$\chi' \le \delta \cdot \chi'_{q^*} \tag{10}$$

as the true "background" cell which will be removed. The value of δ is prescribed. A larger value of δ will reduce the dimension of the unknown vector in the discretized data equation quickly, and thus, the inversion domain is compressed very fast. However, some "scatterer" cells may also be removed. On the contrary, when δ is too small, the inversion domain is compressed slowly, and thus, the effect of MET is negligible.

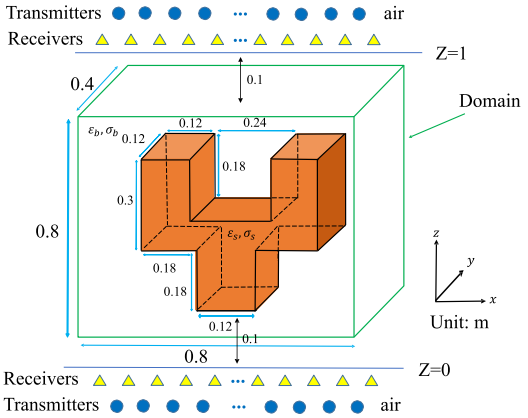

Fig. 2. Configuration of the inversion model with a convex–concave scatterer embedded in the middle layer.

III. Numerical Results

In this section, we present two numerical examples. The first one is used to validate the feasibility as well as the implementation efficiency of the proposed hybrid method by comparing it with the pure VBIM. There is only one homogeneous scatterer in the inversion domain. However, it has an irregular geometrical shape, and two model parameters including the permittivity and conductivity are simultaneously reconstructed. In the second example, there are multiple spheres embedded in the middle layer of a three-layer medium. The permittivity of the big hollow sphere is larger than that of the background medium. However, the permittivity of two solid small spheres is less than that of the background medium. We reconstruct the multiple scatterers to test the antinoise ability of VBIM-MET. In both the numerical examples, the transmitters are unit electric dipoles and polarized at the direction of (1, 1, 1). Such a polarization indicates that three components of the dipole moment in the rectangular coordinate system have the same intensity. The incident fields are computed through the interactions between DGFs and the dipole source current density. The χ'_{max} and χ'_{min} are automatically detected when the VBIM of each iteration outputs the model parameters in all the discretized cells. The parameter M in (8) is set as 150 in both numerical examples. The simulation results show that this value is large enough to guarantee the subintervals small enough and, therefore, to avoid the high risk of incorrect segmentation. The ratio δ in (10) is set as 0.15. The results in the following show that this value can guarantee both the efficiency and stability of VBIM-MET. In order to quantitatively evaluate the performance of the proposed method, we use the data misfit and model misfit defined in (17) and (16) of [4]. They indicate how well the reconstructed scattered field data match the measured data and how well the reconstructed model parameters match the true model parameters. The stop criterion of VBIM iteration is that the data misfit is smaller than 1×10^{-3} or almost keeps unchanged in three successive iterations. All the simulations are performed on a workstation with 20-cores Xeon E2650 v3 2.3 G CPU, 512 GB RAM.

A. Reconstruction of a Convex-Concave Scatterer

As shown in Fig. 2, a convex–concave scatterer is embedded in the middle layer of a three-layer background medium. The top and bottom layers are air, in which the transmitters and receivers are placed. The middle layer has the dielectric parameters $\epsilon_b = 2.0$ and $\sigma_b = 2$ mS/m. The scatterer has the dielectric parameters $\epsilon_s = 3.2$ and $\sigma_s = 6$ mS/m, and its geometry sizes are shown in Fig. 2. The

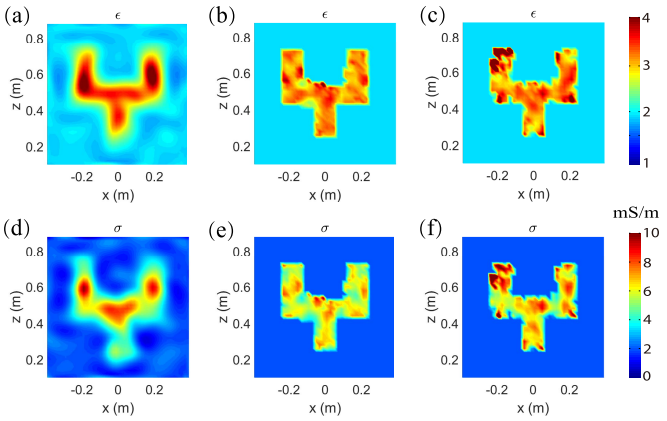

Fig. 3. Detailed xz slices of the reconstructed convex–concave object. (a)–(c) Permittivity profiles from pure VBIM, VBIM-MET, and VBIM enhanced by the middle entropy, respectively. (d)–(f) Conductivity profiles reconstructed by the three methods.

rectangular bulge has the dimensions of 0.12 m × 0.12 m × 0.18 m, and the rectangular gap has the dimensions of 0.24 m × 0.12 m × 0.18 m. About 30 transmitters uniformly locate in two 2.4 m × 1.2 m planes at $z = -0.2$ m and $z = 1.2$ m, respectively. The operating frequency is 300 MHz. The scattered fields are collected by two arrays of 64 receivers uniformly located in two 4.2 m × 1.8 m planes at $z = -0.1$ m and $z = 1.1$ m, respectively. The inversion domain D enclosing the scatterer is discretized into 40 × 20 × 40 cells. The size of each cell is $\Delta x = \Delta y = \Delta z = 0.02$ m. The forward solver BCGS-FFT is used to synthesize the measured scattered fields.

Fig. 3 shows the comparisons of xz slices of the reconstructed convex–concave profiles by VBIM and VBIM-MET. We can see that VBIM-MET outperforms VBIM for both the better reconstructed geometrical shape and more accurate model parameters. As the L_2 norm Tikhonov type regularization is used in the cost function [24], the shapes by VBIM show obvious smoother boundaries. However, this is significantly improved by MET since "background" cells are gradually removed, and thus, the boundaries between the scatterer and background medium are sharply displayed. The removal of the "background" cells also mitigates the ill-posedness of the discretized data equation by reducing the dimension of the vector of unknowns, which finally leads to the more accurate reconstructed permittivity and conductivity. The 2-D profiles reconstructed by VBIM enhanced by the middle entropy are also shown in Fig. 3(c) and (f). Here, the middle entropy is the average value of the maximum entropy and minimum entropy. In other words, we use the middle entropy to distinguish the "scatterer" cells and "background" cells in each VBIM iteration and remove the "background" cells according to (10). Compared with the results shown in Fig. 3(b) and (e) from VBIM-MET, the most obvious feature is that more notches show up in the boundaries of the reconstructed shapes. This is also illustrated by the 3-D isosurfaces of the reconstructed structure shown in Fig. 4. Different from the MET, using the middle entropy to segment the inversion domain does not retain the maximum uncertainty. Consequently, there is a higher risk to incorrectly judge some "scatterer" cells as "background" ones and remove them. This is clearly shown in Fig. 4(b).

Fig. 5(a) shows the convergence curves of data misfits in different iteration steps for pure VBIM, VBIM-MET, and VBIM enhanced by the middle entropy. We can see that the pure VBIM has the smoother convergence curve but the larger final data misfit. When the segmentation of the inversion domain is performed according

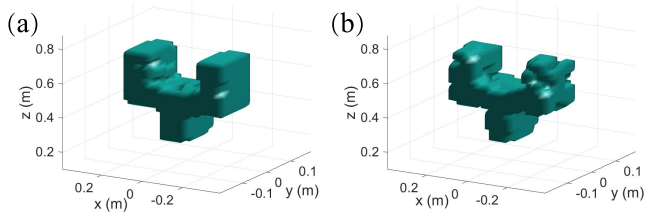

Fig. 4. 3-D isosurface plots of the reconstructed shapes of the convex–concave object. (a) VBIM-MET. (b) VBIM enhanced by middle entropy.

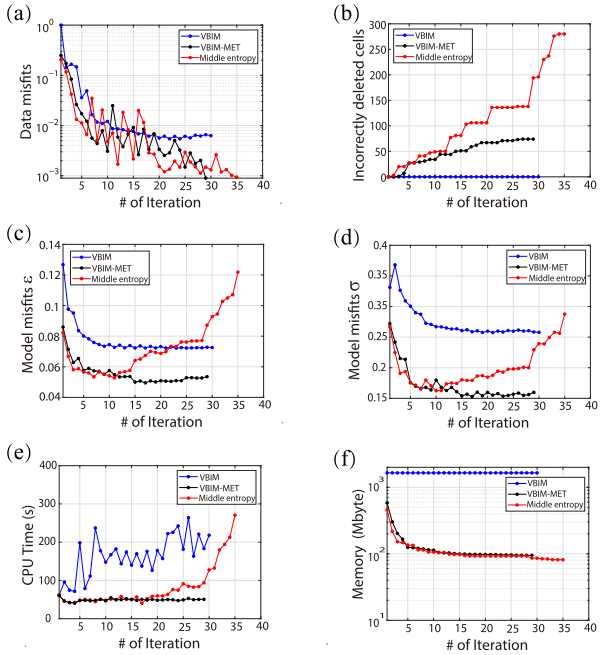

Fig. 5. Computational performance curves for pure VBIM, VBIM-MET, and VBIM enhanced by the middle entropy. (a) Variations of data misfits. (b) Number of cumulatively incorrectly deleted cells. (c) Model misfits of permittivity. (d) Model misfits of conductivity. (e) CPU time in each iteration step. (f) Memory cost in each iteration step.

to maximum or middle entropy and partial "background" cells are removed, the discretized data equations are obligatorily changed in each VBIM iteration. This leads to the unstable oscillations in the convergence curves. However, as the number of unknowns in the discretized data equations is reduced by the removal of "background" cells, the VBIM solver becomes easier to find the optimum solutions of model parameters. As a result, the final data misfits of VBIM-MET or VBIM enhanced by middle entropy are smaller compared with that of the pure VBIM. Fig. 5(b) shows the cumulatively incorrectly deleted cells. In other words, how many "scatterer" cells are incorrectly judged as "background" cells and removed. We can see that the MET no longer incorrectly removes "scatterer" cells when the VBIM iteration approaches the end, i.e., the downsized inversion domain gradually tends to be stable. On the contrary, when the middle entropy is used, the varying inversion domain cannot shrink to a stable region because more and more "scatterer" cells are incorrectly removed. This is also verified by the variations of model misfits shown in Fig. 5(c) and (d). Although the model misfits from VBIM enhanced by MET or the middle entropy are smaller in the first several iteration steps compared with those from the pure VBIM, the model misfit begins to increase quickly later when the middle

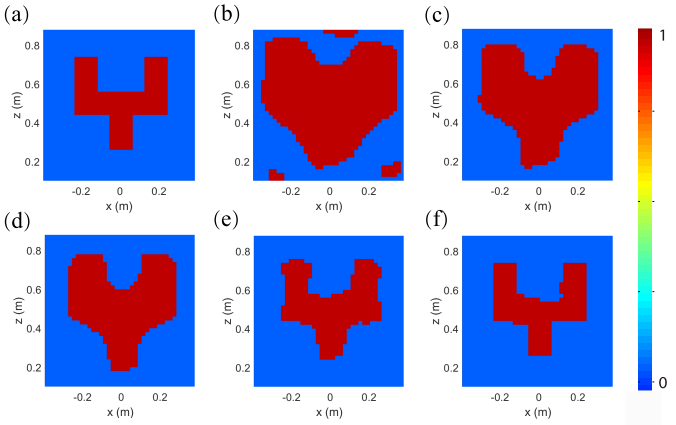

Fig. 6. Detailed xz slices of the segmentation of the inversion domain in different iteration steps of VBIM-MET. (a) Ground truth. (b)–(f) Segmentation in the 1st, 2nd, 3rd, 10th, and 29th steps. The red color denotes the "scatterer" cells, whereas the blue color denotes the "background" cells.

entropy is used to interfere with the VBIM. The middle entropy has no good performance as the maximum entropy. More and more "scatterer" cells in the inversion domain are incorrectly removed, and the reconstructed shape becomes worse and worse. The model misfit automatically becomes larger and larger. Fig. 5(e) and (f) shows the comparisons of computational costs. In each iteration step, when partial "background" cells are removed, the inversion domain is downsized, and fewer unknowns are to be solved by VBIM. Both the time and memory are significantly saved by VBIM-MET or VBIM enhanced by the middle entropy although there is no difference for three different methods at the beginning of the iterations. The quick increase of the time cost shown in the red line of Fig. 5(e) also validates the instability caused by the middle entropy. As too many "scatterer" cells are incorrectly removed and the shape of the scatterer is distorted, it becomes more difficult for the forward solver BCGS-FFT to find the total fields using the scatterer with the severely distorted shape but the true scattered field data. Correspondingly, the time of the forward computation in each iteration increases. Fig. 6 shows the segmentation of the inversion domain in different iteration steps of VBIM-MET. We can see that most "background" cells are removed in several steps at the beginning of iterations. The segmentation gradually approaches stable as the iterations continue. This is consistent with the convergence curves shown in Fig. 5(c).

We then test the robustness of VBIM-MET against the inaccurate background model parameters since their prior information may be not precise in practical applications. Different background parameters are tested in the inversion although the true values are $\epsilon_b = 2.0$ and $\sigma_b = 2$ mS/m. The model misfits of the reconstructed permittivity and conductivity are shown in Table I. We can see that the hybrid reconstruction is rather sensitive to the background parameters. When the parameters change 10% from the true values, e.g., the ϵ_b increases from 2.0 to 2.2, the model misfits of both the reconstructed permittivity and conductivity become several times larger. The inaccurate background parameters make the iterative hybrid solver more difficult to find the well-fitted model parameter distribution. This is compensated by both the deviation of the reconstructed model parameters and the distorted scatterer shapes. As a result, some "background" cells are treated as "scatterer" cells and vice versa. The model misfits will be enlarged. Another interesting observation is that the model misfit of conductivity is larger than that of permittivity. This is because the imaginary part of the complex permittivity which is contributed by the conductivity is obviously smaller than the real part. When both permittivity and conductivity are simultaneously reconstructed from

TABLE I

MODEL MISFITS (%) OF VBIM-MET WHEN THE USED BACKGROUND MODEL PARAMETERS DEVIATE AWAY FROM THE TRUE VALUES

Used ε_b	1.80	1.85	1.90	1.95	2.00	2.05	2.10	2.15	2.20
Used σ_b	2.20	2.15	2.10	2.05	2.00	1.95	1.90	1.85	1.80
Misfits of ε	20.6	18.1	12.7	7.23	5.46	12.8	21.6	34.4	56.8
Misfits of σ	111.6	109.0	96.4	35.1	15.9	49.5	56.8	136.8	159.0

Remark: the unit of σ_b is mS/m.

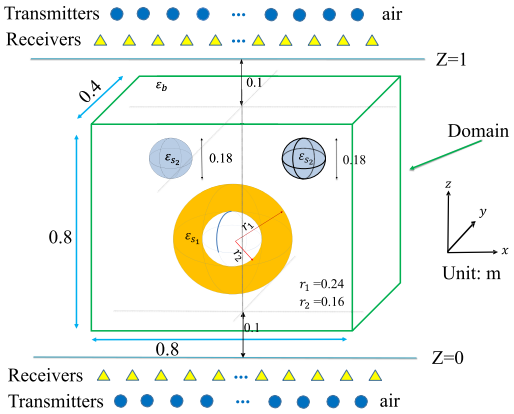

Fig. 7. Configuration of the inversion model with three spheres embedded in the middle layer.

the measured scattered fields, it is more difficult to obtain the precise value of conductivity compared with permittivity.

B. Reconstruction of Multiple Spheres

In this case, we test the antinoise ability of the proposed hybrid VBIM-MET by reconstructing multiple spheres. As shown in Fig. 7, three spheres are embedded in the middle layer of a three-layer medium. The top and bottom layers are air, in which the transmitter and receiver arrays are placed. The layouts of the arrays are the same as those in the first case. The operating frequency is 250 MHz. The middle layer has dielectric parameters $\epsilon_b = 3.2$. Conductivity is not considered. The big sphere has the parameter $\epsilon_s = 4.0$ for the outer layer and $\epsilon_s = 3.2$ for the inner layer. Their radii are 0.24 and 0.16 m, respectively. Two small spheres have the same diameter 0.18 m and the same relative permittivity $\epsilon_s = 2.0$, which is smaller than the background parameter.

Fig. 8 shows the 2-D slices of the reconstructed profiles by VBIM-MET and VBIM when different levels of noise contamination are applied. Here, the noise level is defined as the signal-to-noise ratio (SNR) of power. We can see that VBIM-MET obviously outperforms VBIM. At noise-free condition, the VBIM-MET produces sharp boundaries of three spheres and the clean background profile. On the contrary, three reconstructed spheres by VBIM have blurred boundaries. When 20 dB white Gaussian noise is added, two small spheres reconstructed by VBIM are not discernible. However, they are displayed clearly in the slices produced by VBIM-MET. If we continue to increase the noise level to 10 dB, even the big sphere profile reconstructed by VBIM is severely distorted. Nevertheless, the shapes for all three spheres are basically kept if we use the hybrid VBIM-EM. Table II shows the data misfits and model misfits when the VBIM iterations stop. At the noise-free condition, the final data misfit of VBIM-MET is smaller than that of VBIM. This phenomenon has been discussed in the last case. However, when 20 dB or 10 dB noise is added, the data misfits of both VBIM-MET and VBIM only roughly converge to the amplitude ratio of noise to signal. When the data misfit in the iterations reaches this ratio, it will keep unchanged since it is almost impossible to further adjust the model parameters to match the scattered field data contaminated by random noise. The

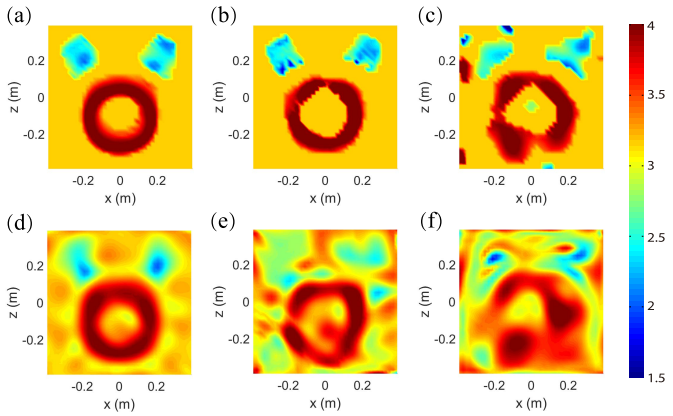

Fig. 8. Detailed xz slices of three reconstructed spheres. (a)–(c) Permittivity profiles reconstructed by VBIM-MET for noise free, 20 dB noise, and 10 dB noise, respectively. (d)–(f) Permittivity profiles reconstructed by pure VBIM for noise free, 20 dB noise, and 10 dB noise, respectively.

TABLE II

FINAL DATA MISFITS AND MODEL MISFITS OF THE RECONSTRUCTION BY VBIM AND VBIM-MET WHEN THE ITERATIONS STOP

SNR \ Misfit	Data misfit(%)		Model misfit(%)	
	VBIM	VBIM-MET	VBIM	VBIM-MET
Noise free	0.207	0.115	11.62	10.70
20 dB Noise	10.3	10.1	14.39	11.61
10 dB Noise	33.4	33.1	28.45	17.46

comparisons of the final model misfits indicate that VBIM-MET has a stronger antinoise ability than VBIM. The higher is the noise level, the more obvious is the discrepancy. When most "background" cells are removed by MET, the inversion domain almost collapses into the "scatterer" subregion. In this situation, the model parameter distribution reconstructed by VBIM is restricted in that subregion. Consequently, the basic shape and parameter values in most cells are still kept although the data are contaminated by noise.

IV. CONCLUSION

In this communication, the statistical method MET is combined with the voxel-based full-wave inversion method VBIM to improve its reconstruction accuracy and lower the computation cost by gradually reducing the dimension of the unknown vector in the discretized data equation. The reduction is realized by segmenting the reconstructed 3-D images into "background" and "scatterer" cells. The confirmed "background" ones are not assembled into the discretized data equation since their model parameters are known. Numerical simulations show that VBIM-MET is superior to VBIM for a higher accuracy of reconstruction, lower computation cost, and stronger antinoise ability. Compared with segmentation using other entropy values, the MET retains the maximum uncertainty, and thus, the VBIM-MET can finally converge to stable model parameters.

REFERENCES

[1] X. Song, M. Li, F. Yang, S. Xu, and A. Abubakar, "Study on joint inversion algorithm of acoustic and electromagnetic data in biomedical imaging," *IEEE J. Multiscale Multiphys. Comput. Techn.*, vol. 4, pp. 2–11, 2019.

[2] Y. Gotoh, M. Tohara, and R. Nakamura, "Electromagnetic inspection for detecting defect of underground part of road sign pillar," *IEEE Trans. Magn.*, vol. 54, no. 11, Nov. 2018, Art. no. 6202304

[3] W. Zhang, A. Hoorfar, C. Thajudeen, and F. Ahmad, "Full polarimetric beam-forming algorithm for through-the-wall radar imaging," *Radio Sci.*, vol. 46, Oct. 2011, Art. no. RS0E16.

[4] T. Lan, N. Liu, F. Han, and Q. H. Liu, "Joint petrophysical and structural inversion of electromagnetic and seismic data based on volume integral equation method," *IEEE Trans. Geosci. Remote Sens.*, vol. 57, no. 4, pp. 2075–2086, Apr. 2019.

[5] M. El-Shenawee, O. Dorn, and M. Moscoso, "An adjoint-field technique for shape reconstruction of 3-D penetrable object immersed in lossy medium," *IEEE Trans. Antennas Propag.*, vol. 57, no. 2, pp. 520–534, Feb. 2009.

[6] O. Dorn and R. Villegas, "A level set method for 3D low frequency electromagnetic imaging with applications in geophysical prospecting," *Proc. Appl. Math. Mech.*, vol. 7, no. 1, pp. 2150023–2150024, Dec. 2007.

[7] M. Li, A. Abubakar, and T. M. Habashy, "A three-dimensional model-based inversion algorithm using radial basis functions for microwave data," *IEEE Trans. Antennas Propag.*, vol. 60, no. 7, pp. 3361–3372, Jul. 2012.

[8] M. Li, A. Abubakar, T. M. Habashy, and Y. Zhang, "Inversion of controlled-source electromagnetic data using a model-based approach," *Geophys. Prospecting*, vol. 58, no. 3, pp. 455–467, May 2010.

[9] L. E. Sun, "Parametric inversion of 3-D anisotropic permittivities from scattered electromagnetic fields," *IEEE Trans. Antennas Propag.*, vol. 66, no. 6, pp. 3027–3033, Jun. 2018.

[10] L. Ding, X. L. Deán-Ben, and D. Razansky, "Real-time model-based inversion in cross-sectional optoacoustic tomography," *IEEE Trans. Med. Imag.*, vol. 35, no. 8, pp. 1883–1891, Aug. 2016.

[11] Z. Q. Zhang and Q. H. Liu, "Three-dimensional nonlinear image reconstruction for microwave biomedical imaging," *IEEE Trans. Biomed. Eng.*, vol. 51, no. 3, pp. 544–548, Mar. 2004.

[12] F. Li, Q. H. Liu, and L.-P. Song, "Three-dimensional reconstruction of objects buried in layered media using Born and distorted Born iterative methods," *IEEE Geosci. Remote Sens. Lett.*, vol. 1, no. 2, pp. 107–111, Apr. 2004.

[13] N. Zaiping, Y. Feng, Z. Yanwen, and Z. Yerong, "Variational Born iteration method and its applications to hybrid inversion," *IEEE Trans. Geosci. Remote Sens.*, vol. 38, no. 4, pp. 1709–1715, Jul. 2000.

[14] L.-P. Song, C. Yu, and Q. H. Liu, "Through-wall imaging (TWI) by radar: 2-D tomographic results and analyses," *IEEE Trans. Geosci. Remote Sens.*, vol. 43, no. 12, pp. 2793–2798, Dec. 2005.

[15] Y. Zhong and X. Chen, "Twofold subspace-based optimization method for solving inverse scattering problems," *Inverse Problems*, vol. 25, no. 8, Aug. 2009, Art. no. 085003.

[16] P. M. V. D. Berg, A. L. V. Broekhoven, and A. Abubakar, "Extended contrast source inversion," *Inverse Problems*, vol. 15, no. 5, pp. 1325–1344, Oct. 1999.

[17] G. Oliveri, P. Rocca, and A. Massa, "A Bayesian-compressive-sampling-based inversion for imaging sparse scatterers," *IEEE Trans. Geosci. Remote Sens.*, vol. 49, no. 10, pp. 3993–4006, Oct. 2011.

[18] G. Oliveri, M. Salucci, N. Anselmi, and A. Massa, "Compressive sensing as applied to inverse problems for imaging: Theory, applications, current trends, and open challenges.," *IEEE Antennas Propag. Mag.*, vol. 59, no. 5, pp. 34–46, Oct. 2017.

[19] S. Caorsi, M. Donelli, D. Franceschini, and A. Massa, "A new methodology based on an iterative multiscaling for microwave imaging," *IEEE Trans. Microw. Theory Techn.*, vol. 51, no. 4, pp. 1162–1173, Apr. 2003.

[20] G. Franceschini, D. Franceschini, and A. Massa, "Full-vectorial three-dimensional microwave imaging through the iterative multiscaling strategy—A preliminary assessment," *IEEE Geosci. Remote Sens. Lett.*, vol. 2, no. 4, pp. 428–432, Oct. 2005.

[21] A. K. C. Wong and P. K. Sahoo, "A gray-level threshold selection method based on maximum entropy principle," *IEEE Trans. Syst., Man, Cybern.*, vol. 19, no. 4, pp. 866–871, Jul. 1989.

[22] J. N. Kapur, P. K. Sahoo, and A. K. C. Wong, "A new method for gray-level picture thresholding using the entropy of the histogram," *Comput. Vis., Graph., Image Process.*, vol. 29, no. 1, pp. 273–285, Jan. 1985.

[23] Y. Chen, P. Wen, F. Han, N. Liu, H. Liu, and Q. H. Liu, "Three-dimensional reconstruction of objects embedded in spherically layered media using variational Born iterative method," *IEEE Geosci. Remote Sens. Lett.*, vol. 14, no. 7, pp. 1037–1041, Jul. 2017.

[24] W. Zhang and Q. H. Liu, "Three-dimensional scattering and inverse scattering from objects with simultaneous permittivity and permeability contrasts," *IEEE Trans. Geosci. Remote Sens.*, vol. 53, no. 1, pp. 429–439, Jan. 2015.

[25] K. A. Michalski and J. R. Mosig, "Multilayered media Green's functions in integral equation formulations," *IEEE Trans. Antennas Propag.*, vol. 45, no. 3, pp. 508–519, Mar. 1997.

[26] F. Han, J. Zhuo, N. Liu, Y. Liu, H. Liu, and Q. H. Liu, "Fast solution of electromagnetic scattering for 3-D inhomogeneous anisotropic objects embedded in layered uniaxial media by the BCGS-FFT method," *IEEE Trans. Antennas Propag.*, vol. 67, no. 3, pp. 1748–1759, Mar. 2019.